




## Stress Constrained Topology Optimization for Void-lattice Infill Structure Design

Yiding Sun <sup>1</sup> , Yun-Fei Fu <sup>2</sup> , Xinming Li <sup>3</sup>  and Yongsheng Ma <sup>4</sup> 

<sup>1</sup> University of Alberta, [yiding1@ualberta.ca](mailto:yiding1@ualberta.ca)

<sup>2</sup> University of Alberta, [yfu15@ualberta.ca](mailto:yfu15@ualberta.ca)

<sup>3</sup> University of Alberta, [xinming1@ualberta.ca](mailto:xinming1@ualberta.ca)

<sup>4</sup> Southern University of Science and Technology, [mays@sustech.edu.cn](mailto:mays@sustech.edu.cn)

Corresponding author: Yongsheng Ma, [mays@sustech.edu.cn](mailto:mays@sustech.edu.cn)  
Xinming Li, [xinming1@ualberta.ca](mailto:xinming1@ualberta.ca)

**Abstract.** This work aims to develop a novel topology optimization method for void-lattice infill structure design by incorporating stress constraints. The ordered SIMP-like stress interpolation is extended to the composite material criterion, and the Tsai-Hill yield criterion-based constraint is constructed. At the same time, the stress measures are properly scaled to reflect the different yield limitations. The global stress constraint, established with the p-norm function, is combined with the stability transformation method to narrow the gap between the p-norm stress and the exact maximum local stress. This work demonstrates the technological details of the stated methodology and substantiates its effectiveness through a classical 2D numerical illustration in mechanical engineering and a lightweight bone-like porous structure design case in medical engineering.

**Keywords:** Topology optimization, Stress constraint, Infill structure, Medical engineering.

**DOI:** <https://doi.org/10.14733/cadaps.2025.322-335>

### 1 INTRODUCTION

Significant strides in additive manufacturing have enabled the production of cellular structures with intricate geometries [1]. Topology Optimization (TO), a practical design tool, has been extensively associated with additive manufacturing due to its ability to generate novel and unforeseen designs under the prescribed objectives and constraints [2-5]. These designs find utility across diverse applications, including medical engineering [6-9], automotive industry [10,11], aerospace [12,13], biomechanics [14], and energy industry [15]. Reducing the weight of a part subjected to stress constraints is able to maximize the strength-to-weight ratio of this component, which has been a pivotal objective in industries. The research investigates the stress constraints within TO, a field where numerous classical approaches have been proposed to tackle challenges in stress-based TO [16-22]. Additionally, the stress-based TO methodology is extended to other material fields like

multiple isotropic materials, anisotropic materials, and hyper elastic materials [23-25]. Combining the TO method with the homogenization theory, the material distribution in multiscale is properly tailored, and the structures with enhanced mechanical performance are achieved. In light of its significance, stress constraints have been investigated within the multiscale TO frameworks in some studies [26-28].

The emulation of bone-like structures in the architectural design of medical engineering presents a compelling avenue for innovation and efficiency. Bone is composed of compact cortical bone and spongy cancellous bone, which form its outer shell and interior. This composite structure arises from a natural optimization process aligning with Wolff's law [29]. Several methodologies have been proposed to emulate and optimize bone-like structures. Liu and Shapiro [30,31] introduced a technique for reconstructing 3D microstructures from 2D samples based on example-based texture synthesis, which could preserve given statistical features. Another approach is about simulating bone tissue adaptation through biology-inspired models, distinctly segregating local and global scales to mimic bone resorption and formation under mechanical stimuli. [32-35]. A study emphasized anisotropic filtering that directs material accumulation in preferred orientations, resembling bone-inspired infills, resulting in enhanced stiffness and robustness. [29,36]. Moreover, Wu et al. [37] presented a computational method that simultaneously optimizes lattice shape and distribution, and it exhibits superior buckling load and mechanical versatility. Frillici and Rotini proposed suitable objective, constraints, and design variables as socket requirements, and they applied shape optimization for the design of prosthesis socket [38]. Additionally, Daynes et al. [39] aligned lattice architectures with principal strain directions to increase the stiffness and intensity of structures. Whereafter they proposed a bio-inspired approach that integrates topology and size optimization, resulting in promising applications across multiple loading case scenarios. [40]. However, other than the mechanical performance challenges encountered in the design for additive manufacturing, computationally economical solutions for mass-customized medical engineering problems are still scarce.

This research aims to propose a stress-constrained TO method for void-lattice infill structure design based on the work by Xu et al. [24]. By extending the ordered Solid Isotropic Material with Penalization (SIMP) like stress interpolation to the composite material criterion, multiple microstructure distributions can be determined on the macro scale, which is an obvious distinction in comparison with the previous work by Xu et al. [24]. In particular, the Tsai-Hill yield criterion-based constraint is established. This attribute presents considerable potential in enhancing mechanical performance, alleviating the structural design complexity, and concomitantly augmenting safety protocols. The remainder of the paper is organized as follows. Section 2 presents the algorithm framework of this method. Then, section 3 validates the proposed method through a 2D benchmark design and a human femur structure. The conclusion is drawn in Section 4.

## 2 ALGORITHM FRAMEWORK

A model needs to be established to ensure the consistency of the yield strength of the microstructure on the microscale and the macroscale stress calculated by the homogenized model on the macroscale. Therefore, the multi-scale failure model is employed to qualify the yield strength of lattice structures with a predefined density ratio. Based on this model, an ordered SIMP stress interpolation is constructed, and a so-called scaling method is adopted to realize the stress constraints for diverse microstructures through one global constraint. For simplicity, in the remaining content, the problem is addressed under 2D orthogonal-isotropic microstructures.

### 2.1 Ordered SIMP Stress Interpolation

The constitutive behaviors of those microstructures need to be obtained to measure the microstructures' stress states in the macroscale. The effective constitutive behaviors of microstructures are mainly governed by their geometric patterns, which can be approximately replaced by an equivalent homogeneous medium. Within a two-dimensional domain, the

homogenized elasticity tensor  $\mathbf{D}_m^H$  of a representative medium volume  $\Omega^m$  (a unit cell) can be calculated by:

$$\mathbf{D}_{m(ijkl)}^H = \frac{1}{\Omega^m} \cdot \sum_{e=1}^n \left[ (\mathbf{u}_e^{A(ij)})^T \mathbf{D}_0 \mathbf{u}_e^{A(ij)} \right], \quad (2.1)$$

where  $\mathbf{u}_e^{A(ij)}$  denotes the microscale element displacement solutions and  $\mathbf{D}_0$  is the elasticity tensor of the base material. As the 2D microstructures utilized in this work are orthogonal-isotropic, only three distinct parameters ( $D_{11}, D_{12}, D_{33}$ ) appear in the elasticity tensor. Three ordered SIMP functions are herein introduced to describe the elasticity tensor interpolation ( $\eta_{11}^E, \eta_{12}^E, \eta_{33}^E$ ), whose detailed expressions refer to the works in [24,41].

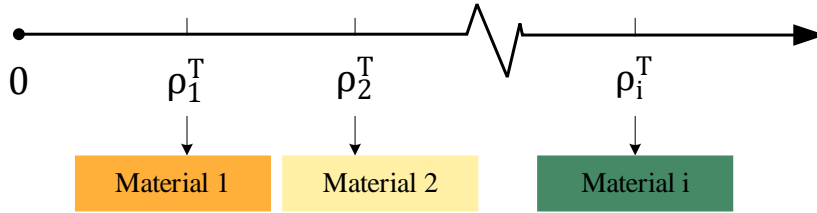


**Figure 1:** Illustration of density-based material sorting.

The ordered SIMP method is employed here to evaluate the properties of composite materials. As depicted in Figure 1, the pseudo isotropic materials are sorted in the ascending order of the material density  $\rho_i^T$ . Then, the material densities are normalized as:

$$\rho_i = \frac{\rho_i}{\rho_{\max}}, \quad (i = 1, 2, 3, \dots, m), \quad (2.2)$$

where  $\rho_{\max}$  is the maximum density among the involved materials,  $m$  is the total number of material phases, and  $\rho_i$  indicates the density of the  $i^{\text{th}}$  lattice structure. The elastic modulus for the element  $e$  ( $E_e$ ) under the multi-material scheme could be formulated by an ordered SIMP interpolation function ( $\eta^E(\rho_e)$ ) as:

$$E_e = \eta^E \cdot (\rho_e) \cdot E_{\max}, \quad (2.3)$$

where  $E_{\max}$  is the elastic modulus for the stiffest material, and  $\rho_e$  is the density of the element  $e$ . Considering the anisotropic properties of lattice structures, the homogenization elastic tensor for the element  $e$  ( $\mathbf{D}_e$ ) could be expressed as:

$$\mathbf{D}_e = \begin{bmatrix} \eta_{11}^E(\rho) \cdot D_{11}^H & \eta_{12}^E(\rho) \cdot D_{12}^H & 0 \\ \eta_{12}^E(\rho) \cdot D_{21}^H & \eta_{11}^E(\rho) \cdot D_{22}^H & 0 \\ 0 & 0 & \eta_{33}^E(\rho) \cdot D_{33}^H \end{bmatrix} = \boldsymbol{\eta}^E(\rho) \cdot \mathbf{D}_{\max}, \quad (2.4)$$

where

$$\boldsymbol{\eta}^E(\rho) = \begin{bmatrix} \eta_{11}^E(\rho) & \eta_{12}^E(\rho) & 0 \\ \eta_{12}^E(\rho) & \eta_{11}^E(\rho) & 0 \\ 0 & 0 & \eta_{33}^E(\rho) \end{bmatrix}, \quad \mathbf{D}_{\max} = \begin{bmatrix} D_{11}^H & D_{12}^H & 0 \\ D_{21}^H & D_{22}^H & 0 \\ 0 & 0 & D_{33}^H \end{bmatrix}, \quad (2.5)$$

$$\boldsymbol{\eta}^E = \left( \frac{\rho_e - \rho_i^T}{\rho_{i+1}^T - \rho_i^T} \right)^p \cdot \left( \frac{\mathbf{D}_{i+1}^H - \mathbf{D}_i^H}{\mathbf{D}_{\max}^H} \right) + \frac{\mathbf{D}_i^H}{\mathbf{D}_{\max}^H}, \quad (2.6)$$

where  $\mathbf{D}_i^H$  is the effective elastic tensor which can be calculated by the homogenization method,  $\mathbf{D}_{\max}^H$  is the stiffest element,  $\boldsymbol{\eta}^E$  is the ordered SIMP interpolation function, and  $p$  is the penalty coefficient. When  $0 < \rho < 1$ , expressions like  $\eta_{11}^E D_{11}^H$  and so forth could be assumed as the components of the elastic tensor for material in intermediate densities described by the ordered SIMP interpolation.

## 2.2 Failure Criterion Identification and Ordered SIMP Stress Interpolation Strategy

For an element with the given density, its Cauchy stress tensor is defined as:

$$\begin{bmatrix} \sigma_x \\ \sigma_y \\ \tau_{xy} \end{bmatrix} = (\boldsymbol{\eta}^E \cdot \mathbf{D}^H) \begin{bmatrix} \varepsilon_x \\ \varepsilon_y \\ \varepsilon_{xy} \end{bmatrix}, \quad (2.7)$$

where  $\sigma_x$ ,  $\sigma_y$ , and  $\tau_{xy}$  are the three stress components of the  $e^{\text{th}}$  element, and  $\varepsilon_x$ ,  $\varepsilon_y$ , and  $\varepsilon_{xy}$  are the three strain components of the  $e^{\text{th}}$  element.

The Tsai-Hill criterion, widely used for anisotropic composite materials, is adopted here to describe the yield behaviors of multiple lattice materials. Firstly, the expression of the Tsai-Hill yield criterion is:

$$\sigma^{T-H} = \left(\frac{\sigma_x}{\bar{\sigma}_X}\right)^2 + \left(\frac{\sigma_y}{\bar{\sigma}_Y}\right)^2 - \frac{\sigma_x \sigma_y}{\bar{\sigma}_X \bar{\sigma}_Y} + \left(\frac{\tau_{xy}}{\bar{\sigma}_{XY}}\right)^2 \leq 1. \quad (2.8)$$

where  $\bar{\sigma}_X$ ,  $\bar{\sigma}_Y$ , and  $\bar{\sigma}_{XY}$  are the yield stress values for the element.

Since the composite structure in this research is assumed to be orthogonal-isotropic, we have  $\sigma_X = \sigma_Y$ . Under this assumption, when we have two materials, the expression of Tsai-Hill yield criterion,  $\sigma^{T-H}$ , can be expressed by the following matrix equation as:

$$\sigma^{T-H} = \boldsymbol{\varepsilon}^T \mathbf{D}^T \mathbf{M} \mathbf{D} \boldsymbol{\varepsilon}, \quad (2.9)$$

where  $\boldsymbol{\varepsilon}$  is the strain and  $\mathbf{M}$  is the criterion matrix, which is given by:

$$\mathbf{M} = \begin{bmatrix} \frac{1}{\bar{\sigma}_X^2} & \frac{1}{2\bar{\sigma}_X \bar{\sigma}_Y} & 0 \\ \frac{1}{2\bar{\sigma}_X \bar{\sigma}_Y} & \frac{1}{\bar{\sigma}_Y^2} & 0 \\ 0 & 0 & \frac{1}{\bar{\sigma}_{XY}^2} \end{bmatrix}, \quad (2.10)$$

Assuming that:

$$\sigma^{T-H}(\rho_i) = \boldsymbol{\varepsilon}^T [(\boldsymbol{\eta}^E(\rho_i) \cdot \mathbf{D}_0)^T (\boldsymbol{\tau}(\rho_i) \cdot \mathbf{M}_0 \cdot \boldsymbol{\tau}(\rho_i)) (\boldsymbol{\eta}^E(\rho_i) \cdot \mathbf{D}_0)] \boldsymbol{\varepsilon}, \quad (2.11)$$

and after replacing the denominators, the Tsai-Hill stress for the weak material is expressed as:

$$\boldsymbol{\tau}(\rho_i) = \begin{bmatrix} \frac{(\bar{\sigma}_X)_0}{(\bar{\sigma}_X)_i} & \frac{\sqrt{(\bar{\sigma}_X)_0 (\bar{\sigma}_Y)_0}}{\sqrt{(\bar{\sigma}_X)_i (\bar{\sigma}_Y)_i}} & 0 \\ \frac{\sqrt{(\bar{\sigma}_X)_0 (\bar{\sigma}_Y)_0}}{\sqrt{(\bar{\sigma}_X)_i (\bar{\sigma}_Y)_i}} & \frac{(\bar{\sigma}_Y)_0}{(\bar{\sigma}_Y)_i} & 0 \\ 0 & 0 & \frac{(\bar{\sigma}_{XY})_0}{(\bar{\sigma}_{XY})_i} \end{bmatrix}. \quad (2.12)$$

Introducing the ordered SIMP functions  $\boldsymbol{\eta}^S$  to interpolate the scaled stress measurements, and then rewrite the Eq. (2.11) as:

$$\sigma^{T-H}(\rho_i) = \boldsymbol{\varepsilon}^T [(\boldsymbol{\eta}^S(\rho_i) \cdot \mathbf{D}_0)^T \mathbf{M}_0 (\boldsymbol{\eta}^S(\rho_i) \cdot \mathbf{D}_0)] \boldsymbol{\varepsilon}, \quad (2.13)$$

where  $\boldsymbol{\eta}^S$  needs to satisfy the following conditions:

$$\boldsymbol{\eta}^S(\rho_i) = \boldsymbol{\eta}^E(\rho_i) \cdot \boldsymbol{\tau}(\rho_i), \quad i = 1, 2, \dots, m. \quad (2.14)$$

At the microscale, the solid material consisting of a lattice structure is assumed to be isotropic with elastic solid of Young's modulus of 1745 MPa, Poisson's ratio of 0.3, and yield strength of 65 MPa.

The expression of  $\sigma^{T-H}$  ensures that when  $\rho_e = \rho_2$ ,  $\sigma^{T-H}(\rho_e)$  indicates the Tsai-Hill measure for the microstructure 2; and when  $\rho_e = \rho_1$ ,  $\sigma^{T-H}(\rho_e)$  indicates the Tsai-Hill measure for the microstructure 1. Apparently, comparing with the real  $\sigma^{T-H}$  calculated by the elastic interpolations ( $\boldsymbol{\eta}^E$ ), the  $\sigma^{T-H}$  calculated by the stress interpolations ( $\boldsymbol{\eta}^S$ ) is enlarged for the weaker microstructure. As a result, the local stress constraints of the two microstructures are expressed as the following global constraint:

$$(\sigma^{T-H})_{\max} \leq 1. \quad (2.15)$$

However, the maximum function is not differentiable. A preferred approach is to use clustering functions to build a single global function that effectively quantifies the maximum stress value, for example, the p-norm function:

$$\sigma^{T-H}_{PN} = \left( \sum_{e=1}^{Nel} (\sigma^{T-H}(\rho_e))^P \right)^{\frac{1}{P}} \leq 1, \quad (2.16)$$

where  $\sigma_{PN}$  is the global P-norm measure, P is the aggregation parameter, and Nel is the total number of elements. Note that the P-norm approaches the maximum stress  $(\sigma^{T-H})_{\max}$  when  $P \rightarrow \infty$ . However, a large P value tends to make the stress constrained problem erroneous. Relatively small P value is preferred in practice under given convergence stability which, however, leads to the gap between the exact and the approximated maximum stresses. Consequently, the stress constrained optimization result is conservative. Therefore, to better approximate the maximum stress without overly increasing the P value, the global P-norm stress measure is iteratively corrected through:

$$\bar{\sigma}^{T-H}_{PN} = c \cdot \sigma^{T-H}_{PN}, \quad (2.17)$$

where c is the correction parameter at the  $I^{th}$  iteration ( $I > 1$ ) that reflects the ratio of the maximum von Mises stress to the P-norm stress of the current iteration. It is noted that the parameter c may result in abrupt fluctuations if only relying on the history-independent stress ratio to correct, potentially leading to numerical oscillations and instabilities. To address this issue, a parameter  $\alpha^I$  ( $\alpha^I \in (0,1]$ ) is introduced to restrict the variation between  $c^I$  and  $c^{I-1}$ , as demonstrated by:

$$c^I = \alpha^I \cdot \frac{\max(\forall \sigma_{vm,e})}{\sigma_{PN}^I} + (1 - \alpha^I) \cdot c^{I-1}. \quad (2.18)$$

Here,  $\alpha^I = 0.5$  is adopted for all iterations, and  $c^0 = 1$  is selected. Note that the set of local stress constraints is equivalent to one constraint under the maximum local stress, which is described as:

$$\bar{\sigma}^{T-H}_{PN} \leq 1. \quad (2.19)$$

### 2.3 Optimization Problem Formulation

The objective function is to minimize the structure weight subject to the maximum Tsai-Hill stress constraint. The optimization problem can be mathematically formulated as:

$$\begin{cases} \text{find: } \boldsymbol{\rho} \\ \text{minimize: } M(\boldsymbol{\rho}) = \sum_{e=1}^{Nel} \bar{\rho}_e \\ \text{subject to: } \begin{cases} \mathbf{KU} = \mathbf{F} \\ \bar{\sigma}^{T-H}_{PN} \leq 1 \\ \rho_{\min} \leq \forall \bar{\rho}_e \leq 1 \end{cases} \end{cases}, \quad (2.20)$$

where  $M(\boldsymbol{\rho})$  is the objective function of the optimization problem, which represents the total mass of the structure.  $\mathbf{K}$ ,  $\mathbf{U}$  and  $\mathbf{F}$  in the equilibrium equation denote stiffness matrix, global displacement and prescribed external loads, respectively. The filtered design variable  $\forall \bar{\rho}_e$  is limited by the upper bound 1, and the lower bound  $\rho_{\min}$ . The stress measure is the P-norm form formulated using the Tsai Hill's stress. After obtaining the gradient of this model, the Method of Moving Asymptotes (MMA) is adopted to update the topological configuration iteratively. Hence, details of sensitivity analysis are presented in the following. The gradient of the mass objective function M is:

$$\frac{\partial M}{\partial \bar{\rho}_j} = \sum_{e=1}^{Nel} \left( \frac{\partial \bar{\rho}_e}{\partial \bar{\rho}_j} \cdot m_0 \right), \quad (2.21)$$

where  $\frac{\partial \bar{\rho}_e}{\partial \bar{\rho}_j} \neq 0$  only stands for  $j = e$ . Thus, the sum operation in Eq. (2.21) can be removed, and the functions are represented as:

$$\frac{\partial M}{\partial \bar{\rho}_j} = m_0, \quad (2.22)$$

$$\frac{\partial \bar{\sigma}^{T-H}_{PN}}{\partial \bar{\rho}_j} = \sum_{e=1}^{Nel} \left[ \frac{\partial \bar{\sigma}^{T-H}_{PN}}{\partial \sigma^{T-H}_e} \frac{\partial \sigma^{T-H}_e}{\partial \bar{\rho}_j} \right], \quad (2.23)$$

$$\frac{\partial \overline{\sigma}^{\text{T-H}}_{\text{PN}}}{\partial \sigma^{\text{T-H}}_e} = c \cdot \frac{1}{P} \cdot \left[ \sum_{e=1}^{\text{Nel}} (\sigma^{\text{T-H}}_e)^P \right]^{\left(\frac{1}{P}-1\right)} \cdot P \cdot (\sigma^{\text{T-H}}_e)^{(P-1)}, \quad (2.24)$$

$$\frac{\partial \sigma^{\text{T-H}}_e}{\partial \bar{\rho}_j} = \frac{\partial \boldsymbol{\varepsilon}^{\text{T}} \left[ (\boldsymbol{\eta}^{\text{S}} \cdot \mathbf{D}_0)^{\text{T}} \mathbf{M}_0 (\boldsymbol{\eta}^{\text{S}} \cdot \mathbf{D}_0) \right] \boldsymbol{\varepsilon}}{\partial \bar{\rho}_j}, \quad (2.25)$$

then we have:

$$\frac{\partial \sigma^{\text{T-H}}_e}{\partial \bar{\rho}_j} = 2 \boldsymbol{\varepsilon}^{\text{T}} \left[ (\boldsymbol{\eta}^{\text{S}} \cdot \mathbf{D}_0)^{\text{T}} \mathbf{M}_0 (\boldsymbol{\eta}^{\text{S}} \cdot \mathbf{D}_0) \right] \frac{\partial \boldsymbol{\varepsilon}}{\partial \bar{\rho}_j} + \boldsymbol{\varepsilon}^{\text{T}} \frac{\partial \left[ (\boldsymbol{\eta}^{\text{S}} \cdot \mathbf{D}_0)^{\text{T}} \mathbf{M}_0 (\boldsymbol{\eta}^{\text{S}} \cdot \mathbf{D}_0) \right]}{\partial \bar{\rho}_j} \boldsymbol{\varepsilon}, \quad (2.26)$$

where

$$\boldsymbol{\varepsilon}^{\text{T}} \frac{\partial \left[ (\boldsymbol{\eta}^{\text{S}} \cdot \mathbf{D}_0)^{\text{T}} \mathbf{M}_0 (\boldsymbol{\eta}^{\text{S}} \cdot \mathbf{D}_0) \right]}{\partial \bar{\rho}_j} \boldsymbol{\varepsilon} = 2 \boldsymbol{\varepsilon}^{\text{T}} \left[ \left( \frac{\partial \boldsymbol{\eta}^{\text{S}}}{\partial \bar{\rho}_j} \cdot \mathbf{D}_0 \right)^{\text{T}} \mathbf{M}_0 (\boldsymbol{\eta}^{\text{S}} \cdot \mathbf{D}_0) \right] \boldsymbol{\varepsilon}. \quad (2.27)$$

According to the strain-displacement formulation, the macroscopic strain tensor on an element is computed as:

$$\boldsymbol{\varepsilon} = \mathbf{B} \mathbf{u}_e, \quad (2.28)$$

where  $\mathbf{B}$  represents strain-displacement matrix and  $\mathbf{u}_e$  is the displacement vector of the  $e^{\text{th}}$  element. Substituting Eq. (2.28) into the second term in Eq. (2.26), the derivatives can be expressed as:

$$\frac{\partial \overline{\sigma}^{\text{T-H}}_{\text{PN}}}{\partial \bar{\rho}_j} = \sum_{e=1}^{\text{Nel}} \left[ \frac{\partial \overline{\sigma}^{\text{T-H}}_{\text{PN}}}{\partial \sigma^{\text{T-H}}_e} \left( 2 \boldsymbol{\varepsilon}^{\text{T}} \left[ (\boldsymbol{\eta}^{\text{S}} \cdot \mathbf{D}_0)^{\text{T}} \mathbf{M}_0 (\boldsymbol{\eta}^{\text{S}} \cdot \mathbf{D}_0) \right] \mathbf{B} \frac{\partial \mathbf{u}_e}{\partial \bar{\rho}_j} + 2 \boldsymbol{\varepsilon}^{\text{T}} \left[ \left( \frac{\partial \boldsymbol{\eta}^{\text{S}}}{\partial \bar{\rho}_j} \cdot \mathbf{D}_0 \right)^{\text{T}} \mathbf{M}_0 (\boldsymbol{\eta}^{\text{S}} \cdot \mathbf{D}_0) \right] \boldsymbol{\varepsilon} \right) \right]. \quad (2.29)$$

Knowing that  $\frac{\partial \boldsymbol{\eta}^{\text{S}}_e}{\partial \bar{\rho}_j} \neq 0$  only implies that  $j = e$ . Thus, the sum operation in Eq. (2.29) is converted as:

$$\begin{aligned} \frac{\partial \overline{\sigma}^{\text{T-H}}_{\text{PN}}}{\partial \bar{\rho}_j} &= \sum_{e=1}^{\text{Nel}} \left[ \frac{\partial \overline{\sigma}^{\text{T-H}}_{\text{PN}}}{\partial \sigma^{\text{T-H}}_e} \left( 2 \boldsymbol{\varepsilon}^{\text{T}} \left[ (\boldsymbol{\eta}^{\text{S}} \cdot \mathbf{D}_0)^{\text{T}} \mathbf{M}_0 (\boldsymbol{\eta}^{\text{S}} \cdot \mathbf{D}_0) \right] \mathbf{B} \frac{\partial \mathbf{u}_e}{\partial \bar{\rho}_j} \right) \right. \\ &\quad \left. + \frac{\partial \overline{\sigma}^{\text{T-H}}_{\text{PN}}}{\partial \sigma^{\text{T-H}}_j} \left( 2 \boldsymbol{\varepsilon}^{\text{T}} \left[ \left( \frac{\partial \boldsymbol{\eta}^{\text{S}}}{\partial \bar{\rho}_j} \cdot \mathbf{D}_0 \right)^{\text{T}} \mathbf{M}_0 (\boldsymbol{\eta}^{\text{S}} \cdot \mathbf{D}_0) \right] \boldsymbol{\varepsilon} \right) \right]. \end{aligned} \quad (2.30)$$

The adjoint method is then adopted to address the unknown term in Eq. (2.30). Specifically, taking derivatives of both sides of  $\mathbf{K}\mathbf{U} = \mathbf{F}$  yields:

$$\frac{\partial \mathbf{K}}{\partial \bar{\rho}_j} \mathbf{U} + \mathbf{K} \frac{\partial \mathbf{U}}{\partial \bar{\rho}_j} = 0. \quad (2.31)$$

Subsequently, the following expression is derived as:

$$\frac{\partial \mathbf{U}}{\partial \bar{\rho}_j} = -\mathbf{K}^{-1} \frac{\partial \mathbf{K}}{\partial \bar{\rho}_j} \mathbf{U}, \quad (2.32)$$

and the above derivative is further transcribed as:

$$\frac{\partial \mathbf{u}_e}{\partial \bar{\rho}_j} = -\mathbf{L}_e \mathbf{K}^{-1} \frac{\partial \mathbf{K}}{\partial \bar{\rho}_j} \mathbf{U}, \quad (2.33)$$

where  $\mathbf{L}_e$  is the global-local transform matrix, which extracts the nodal displacements of the  $e^{\text{th}}$  element from the global displacement vector through  $\mathbf{u}_e = \mathbf{L}_e \mathbf{U}$ . Then, we have:

$$\begin{aligned} &\sum_{e=1}^{\text{Nel}} \left[ \frac{\partial \overline{\sigma}^{\text{T-H}}_{\text{PN}}}{\partial \sigma^{\text{T-H}}_e} \left( 2 \boldsymbol{\varepsilon}^{\text{T}} \left[ (\boldsymbol{\eta}^{\text{S}} \cdot \mathbf{D}_0)^{\text{T}} \mathbf{M}_0 (\boldsymbol{\eta}^{\text{S}} \cdot \mathbf{D}_0) \right] \mathbf{B} \frac{\partial \mathbf{u}_e}{\partial \bar{\rho}_j} \right) \right] = \\ &- \sum_{e=1}^{\text{Nel}} \left[ \frac{\partial \overline{\sigma}^{\text{T-H}}_{\text{PN}}}{\partial \sigma^{\text{T-H}}_e} \left( 2 \boldsymbol{\varepsilon}^{\text{T}} \left[ (\boldsymbol{\eta}^{\text{S}} \cdot \mathbf{D}_0)^{\text{T}} \mathbf{M}_0 (\boldsymbol{\eta}^{\text{S}} \cdot \mathbf{D}_0) \right] \mathbf{B} \mathbf{L}_e \mathbf{K}^{-1} \right) \right] \frac{\partial \mathbf{K}}{\partial \bar{\rho}_j} \mathbf{U}. \end{aligned} \quad (2.34)$$

Adopting the vector  $\boldsymbol{\lambda} = \sum_{e=1}^{\text{Nel}} \boldsymbol{\lambda}_e$  to indicate the adjoint vector in Eq. (2.34):

$$\boldsymbol{\lambda}_e = \left[ \frac{\partial \overline{\sigma}^{\text{T-H}}_{\text{PN}}}{\partial \sigma^{\text{T-H}}_e} \left( 2 \boldsymbol{\varepsilon}^{\text{T}} \left[ (\boldsymbol{\eta}^{\text{S}} \cdot \mathbf{D}_0)^{\text{T}} \mathbf{M}_0 (\boldsymbol{\eta}^{\text{S}} \cdot \mathbf{D}_0) \right] \mathbf{B} \mathbf{L}_e \mathbf{K}^{-1} \right) \right], \quad (2.35)$$

and it is calculated from the following adjoint expression:

$$\mathbf{K} \boldsymbol{\lambda} = \mathbf{f}, \quad (2.36)$$

where the adjoint force vector is obtained as:

$$\mathbf{f} = \sum_{e=1}^{Nel} \left[ \frac{\partial \overline{\sigma}^{T-H}_{PN}}{\partial \sigma^{T-H}_e} \left( 2\boldsymbol{\varepsilon}^T \left[ (\boldsymbol{\eta}^S \cdot \mathbf{D}_0)^T \mathbf{M}_0 (\boldsymbol{\eta}^S \cdot \mathbf{D}_0) \right] \mathbf{B} \mathbf{L}_e \right) \right]. \quad (2.37)$$

Then, Eq. (2.34) is written as:

$$\sum_{e=1}^{Nel} \left[ \frac{\partial \overline{\sigma}^{T-H}_{PN}}{\partial \sigma^{T-H}_e} \left( 2\boldsymbol{\varepsilon}^T \left[ (\boldsymbol{\eta}^S \cdot \mathbf{D}_0)^T \mathbf{M}_0 (\boldsymbol{\eta}^S \cdot \mathbf{D}_0) \right] \mathbf{B} \frac{\partial \mathbf{u}_e}{\partial \bar{\rho}_j} \right) \right] = -\boldsymbol{\lambda}^T \frac{\partial \mathbf{K}}{\partial \bar{\rho}_j} \mathbf{U}. \quad (2.38)$$

The global stiffness matrix could be expressed with the adaptation of the transform matrix  $\mathbf{L}_e$ , which has the form:

$$\mathbf{K} = \sum_{e=1}^{Nel} (\mathbf{L}_e^T \mathbf{K}_e \mathbf{L}_e) = \sum_{e=1}^{Nel} (\mathbf{L}_e^T \delta(\overline{\boldsymbol{\eta}}^E \cdot \mathbf{D}_0) \mathbf{L}_e), \quad (2.39)$$

where  $\mathbf{K}_e$  is the element stiffness matrix for the  $e^{\text{th}}$  element, and  $\delta(*)$  is the element stiffness matrix assembly operator. Thus, the derivative of the global stiffness matrix with respect to  $\bar{\rho}_j$  equals:

$$\frac{\partial \mathbf{K}}{\partial \bar{\rho}_j} = \sum_{e=1}^{Nel} \left( \mathbf{L}_e^T \delta \left( \frac{\partial \overline{\boldsymbol{\eta}}^E}{\partial \bar{\rho}_j} \cdot \mathbf{D}_0 \right) \mathbf{L}_e \right). \quad (2.40)$$

Similar with Eq. (2.21),  $\frac{\partial \overline{\boldsymbol{\eta}}^E}{\partial \bar{\rho}_j} \neq 0$  only stands for  $j = e$ . Hence, the sum operation is removed, and Eq. (2.40) becomes:

$$\frac{\partial \mathbf{K}}{\partial \bar{\rho}_j} = \mathbf{L}_j^T \delta \left( \frac{\partial \overline{\boldsymbol{\eta}}^E}{\partial \bar{\rho}_j} \cdot \mathbf{D}_0 \right) \mathbf{L}_j, \quad (2.41)$$

Therefore, the derivative of the global P-norm stress measure with respect to the design variable is expressed by:

$$\frac{\partial \overline{\sigma}^{T-H}_{PN}}{\partial \bar{\rho}_j} = -\boldsymbol{\lambda}^T \mathbf{L}_j^T \delta \left( \frac{\partial \overline{\boldsymbol{\eta}}^E}{\partial \bar{\rho}_j} \cdot \mathbf{D}_0 \right) \mathbf{L}_j \mathbf{U} + \frac{\partial \overline{\sigma}^{T-H}_{PN}}{\partial \sigma^{T-H}_j} \left( 2\boldsymbol{\varepsilon}^T \left[ \left( \frac{\partial \boldsymbol{\eta}^S}{\partial \bar{\rho}_j} \cdot \mathbf{D}_0 \right)^T \mathbf{M}_0 (\boldsymbol{\eta}^S \cdot \mathbf{D}_0) \right] \boldsymbol{\varepsilon} \right). \quad (2.42)$$

### 3 CASE STUDY

The commercial software package MATLAB is used to implement Finite Element Analysis (FEA) and topology optimization in this study. All numerical experiments are implemented on a computer with an x64-based processor.

#### 3.1 2D Benchmark Case

The proposed method is first validated with a 2D L-bracket case. It is noted that the L-bracket case is extensively adopted to demonstrate stress-related topology optimization algorithms. For all numerical examples, 4-node quadrilateral elements are adopted. The default move limit of 0.5 is used in the MMA optimizer. The initial design variable value in this case is set to be 0.3, and the filter radius is 3.5 element sizes. The optimization process will be converged when no further enhancement of the objectives is attainable. That is, when the difference of the objective values between two adjacent iterations is less than 0.01 over 20 steps or when the maximum iteration number, which is set to 450, is exceeded.

The boundary and loading conditions of the L-bracket case are demonstrated in Figure 2. The structured rectangular mesh with the 1st-order Lagrange elements is adopted in this case. The mesh dimension is  $50 \times 50$  elements in the macroscale and  $50 \times 50$  elements in the microscale and the homogenized stress state is calculated at the element centroid. It is noted that the selection of  $50 \times 50$  is a trade-off between the accuracy and efficiency of the algorithm. The top edge of the L-bracket is clamped and a vertical load  $F=4500$  N is exerted to the right-side upper corner, as shown in Figure 2. Note that the load is distributed over 6 nodes to avoid the stress concentration.

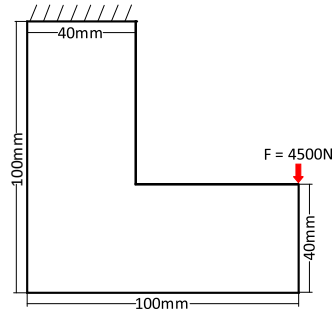


**Figure 2:** Boundary and loading conditions of L-bracket.

The two microstructures are made by one isotropic material, whose yield strength is 65 MPa and Young’s Modulus is 1050 MPa. The mechanical properties of the two pre-designed microstructures are listed in Table 1.

Microstructure 1		Density ratio	Yield strength in x direction (MPa)	Yield strength in xy direction (MPa)
		60%	1650	750
		$D_{11}$	$D_{12}$	$D_{33}$
		$3.8681e5$	$1.5835e5$	$8.8424e4$
Microstructure 2		Density ratio	Yield strength in x direction	Yield strength in xy direction
		40%	1250	667
		$D_{11}$	$D_{12}$	$D_{33}$
		$1.7575e5$	$1.2116e5$	$3.9591e4$

**Table 1:** Mechanical properties of two pre-designed microstructures.

The interpolation curves of the normalized elastic modulus and normalized and scaled stress modulus with respect to the density variables are shown in Figure 3.

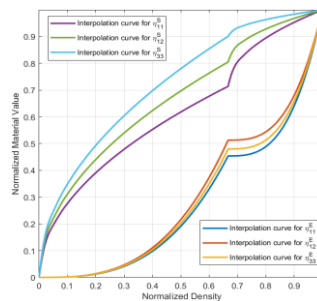


**Figure 3:** Interpolation curves for  $\eta^S$  and  $\eta^E$ .



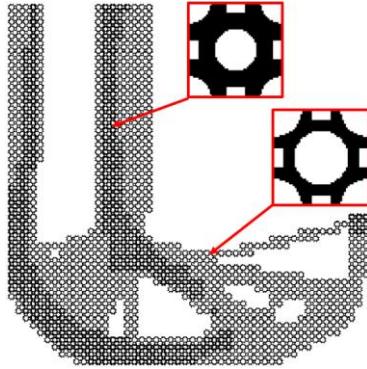


**Figure 4:** Final result of full-scale design.

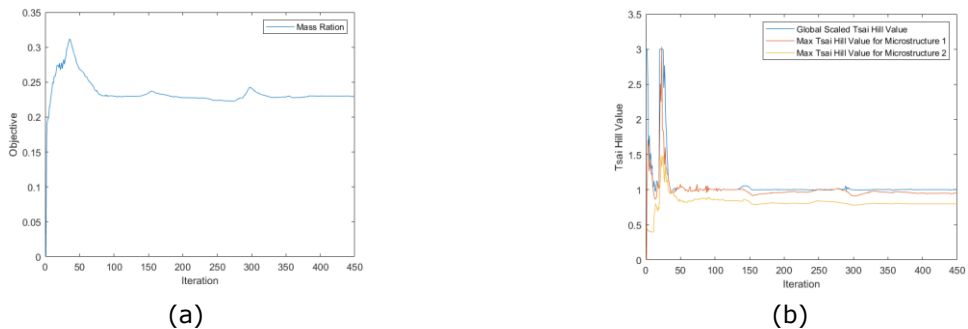


**Figure 5:** (a) Convergence history of the objective value, and (b) convergence history of the Tsai-Hill stress constraints.

The optimized structure of full-scale design is shown in Figure 4. The stress evaluation and objective value histories for this case are plotted in Figure 5. It can be observed that the stress constraints in both microstructures are well satisfied, even though there are severe numerical oscillations occurred during the optimization process. The optimization terminates at the 450<sup>th</sup> iteration, which reaches the final mass ratio of 0.2347. Moreover, the maximum Tsai-Hill stress in microstructure 1 and microstructure 2 are 0.9482 and 0.8011, respectively.

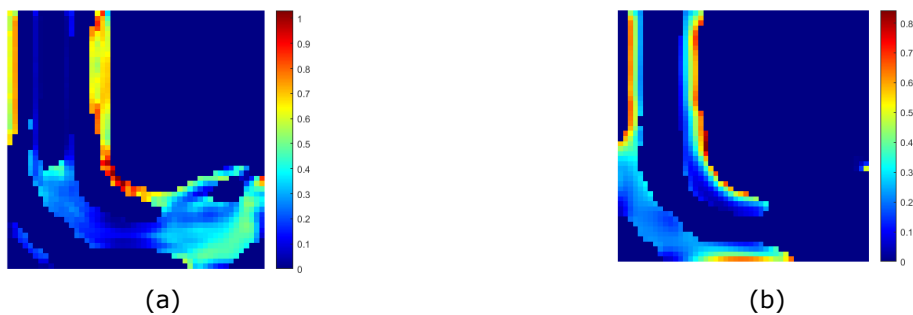


**Figure 6:** Tsai-Hill stress distributions for (a) microstructure two and (b) microstructure 1.

Figure 6 shows the real Tsai-Hill stress distributions for different microstructure phases. It is observed that the resulting structure suffers from a significant stress concentration around the reentrant corner for microstructure 2, as shown in Figure 6(a); while the highest stress occurred at the bottom area of the bracket for microstructure 1, as shown in Figure 6(b).

### 3.2 Bone-like Case

The proposed approach is subsequently validated using a bone-like case as a complex structure example meanwhile the two microstructures listed in Table 1 are applied in this case. The domestic design domain and its boundary conditions for a human femur structure are shown in Figure 7. It should be noted that this optimization case dismisses the biological and medical considerations regarding tissue growth and the practicalities of medical manufacturing.

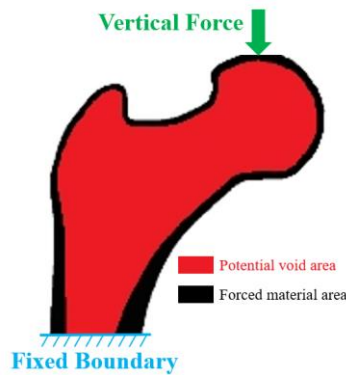


**Figure 7:** Design domain and boundary conditions subjected to single load case.

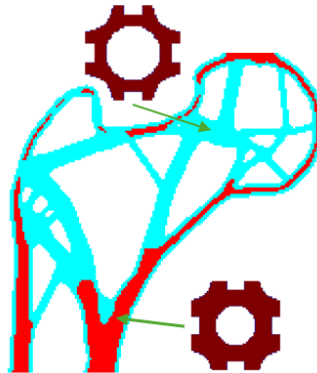


**Figure 8:** Result of bone-like case.

The optimized bone structure is shown in Figure 8, and Figure 9 depicts the real Tsai-Hill stress distributions for different microstructure phases. The final mass ratio of the optimized design reaches 0.2644. Figure 9(a) indicates the stress distribution for microstructure 2, while Figure 9 (b) indicates the stress distribution for microstructure 1 for a human femur structure. The maximum Tsai-Hill stresses in two microstructures are 0.9981 and 0.8113, respectively.

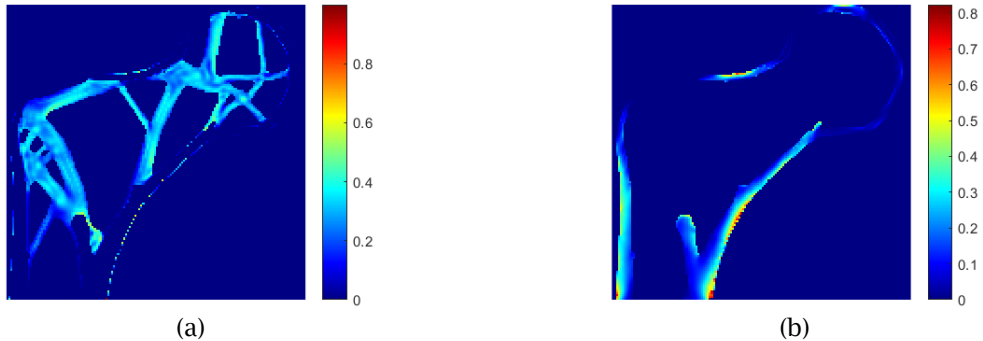


**Figure 9:** Tsai-Hill stress distributions for (a) microstructure 2 and (b) microstructure 1 for a human femur structure.

The results show that this method enables the reliable, lightweight design of the target human femur structure, ensuring a weight reduction of up to 75% while still meeting the strength requirements of the material.

#### 4 CONCLUSIONS

A framework of stress-based topology optimization is proposed for void-lattice infill structure design in additive manufacturing. The novelty of this work is that instead of simply using the SIMP material interpolation, the homogenization method is employed to efficiently obtain the effective mechanical properties of lattice structures, ensuring compliance with maximum stress requirements. An ordered SIMP-like stress interpolation is developed, which is suitable for the Tsai-Hill failure criterion in multiscale simulation. In other words, for the effectiveness of yield strength, the modified Tsai-Hill's yield criterion is applied to estimate the mechanical performance of lattice structures. A representative L-bracket case is provided to demonstrate the validation of this study. Moreover, this methodology is also implemented in bone-like porous structures. In both cases, the proposed approach employs multiscale stress-constrained ordered SIMP interpolation as an innovative algorithmic approach. Moreover, augmenting safety protocols is accomplished with modularized data management and enhanced structural robustness through the optimization process. This optimization methodology iteratively optimizes the material distributions from the design domain while maintaining its mechanical properties under given loadings, achieving an optimal structure with desired mechanical performance.

The proposed algorithm framework is versatile for optimization processes in almost any simulation environment. It is primarily implemented in 2D void-lattice infill structure design but is adaptable to 3D with increased computational requirements. These ordered SIMP-like stress interpolation designs have limited degrees of freedom and exhibit relatively poor performance in the face of multiple microstructural variations. Moreover, the optimization of bone-like structures serves merely as an example within the domain of lightweight complex structures, offering insights applicable to related fields. Clarifying the optimization objectives and addressing customer needs, which brings corresponding mechanics, optimization rules, and material information on demand according to the customized conditions, is critical to the digitalization and mass customization of lightweight structures in the engineering industry. The future work will develop a modularized and real-time data link that contributes to the seamless synchronization of software information throughout the organizations, especially for the mass customization in additive manufacturing, namely, the complex structure development. In addition, topology optimization of 3D void-lattice infill structure design cases will be conducted with a newly developed optimization platform based

on Smooth-Edged Material Distribution for Optimizing Topology algorithm, with the aim of obtaining more practical and manufacturable designs.

Yiding Sun, <https://orcid.org/0000-0002-5469-3151>  
 Yun-Fei Fu, <https://orcid.org/0000-0003-0058-2349>  
 Xinming Li, <https://orcid.org/0000-0001-6802-033X>  
 Yongsheng Ma, <https://orcid.org/0000-0002-6155-0167>

## REFERENCES

- [1] Duncan, O.; Shepherd, T.; Moroney, C.; Foster, L.; Venkatraman, P. D.; Winwood, K.; Allen, T.; Alderson, A.: Review of auxetic materials for sports applications: Expanding options in comfort and protection, *Applied Sciences (Switzerland)* 8, 2018. <https://doi.org/10.3390/app8060941>.
- [2] Bendsoe, M.P.: Optimal shape design as a material distribution problem, *Structural Optimization* 1, 1989, 193–202. <https://doi.org/10.1007/BF01650949>.
- [3] Fu, Y. F.; Long, K.; Rolfe, B.: 2023. On non-penalization SEMDOT using discrete variable sensitivities. *Journal of Optimization Theory and Applications*, 198(2), 2023, 644–677. <https://doi.org/10.1007/s10957-023-02222-3>.
- [4] Liu, J.; Gaynor, A. T.; Chen, S.; Kang, Z.; Suresh, K.; Takezawa, A.; Li, L.; Kato, J.; Tang, J.; Wang, C. C. L.; Cheng, L.; Liang, X.; To, Albert. C.: Current and future trends in topology optimization for additive manufacturing, *Structural and Multidisciplinary Optimization*, 57, 2018, 2457–2483. <https://doi.org/10.1007/s00158-018-1994-3>.
- [5] Cardillo, A.; Cascini, G.; Frillici, F. S.; Rotini, F.: Multi-objective topology optimization through GA-based hybridization of partial solutions, *Engineering with Computers*, 29, 2013, 287–306. <https://doi.org/10.1007/s00366-012-0272-z>.
- [6] Jardini, A. L.; Larosa, M. A.; Filho, R. M.; Zavaglia, C. A. de C.; Bernardes, L. F.; Lambert, C. S.; Calderoni, D. R.; Kharmandayan, P.: Cranial reconstruction: 3D biomodel and custom-built implant created using additive manufacturing, *Journal of Cranio-Maxillofacial Surgery*, 42, 2014, 1877–1884. <https://doi.org/10.1016/j.jcms.2014.07.006>.
- [7] Stübinger, S.; Mosch, I.; Robotti, P.; Sidler, M.; Klein, K.; Ferguson, S. J.; von Rechenberg, B.: Histological and biomechanical analysis of porous additive manufactured implants made by direct metal laser sintering: A pilot study in sheep, *Journal of Biomedical Materials Research Part B: Applied Biomaterials*, 101(7), 2013, 1154–1163. <https://doi.org/10.1002/jbm.b.32925>.
- [8] Yan, Q.; Dong, H.; Su, J.; Han, J.; Song, B.; Wei, Q.; Shi, Y.: A Review of 3D Printing Technology for Medical Applications, *Engineering*, 4, 2018, 729–742. <https://doi.org/10.1016/j.eng.2018.07.021>.
- [9] Mahmoud, D.; Elbestawi, M.: Lattice Structures and Functionally Graded Materials Applications in Additive Manufacturing of Orthopedic Implants: A Review. *Journal of Manufacturing and Materials Processing*, 1, 2017, 13. <https://doi.org/10.3390/jmmp1020013>.
- [10] Abdi, M.; Ashcroft, I.; Wildman, R. D.: Design optimisation for an additively manufactured automotive component, *International Journal of Powertrains*, Vol. 7, Issue 3, 2018. <https://doi.org/10.1504/IJPT.2018.090371>.
- [11] Walton, D.; Moztarzadeh, H.: Design and Development of an Additive Manufactured Component by Topology Optimisation, *Procedia CIRP*, Elsevier B.V., 2017, pp. 205–210. <https://doi.org/10.1016/j.procir.2017.03.027>.
- [12] Türk, D. A.; Kussmaul, R.; Zogg, M.; Klahn, C.; Leutenecker-Twelsiek, B.; Meboldt, M.: Composites Part Production with Additive Manufacturing Technologies, *Procedia CIRP*, Elsevier B.V., 2017, pp. 306–311. <https://doi.org/10.1016/j.procir.2017.03.359>.
- [13] Orme, M. E.; Gschweidl, M.; Ferrari, M.; Madera, I.; Mouriaux, F.: Designing for Additive Manufacturing: Lightweighting Through Topology Optimization Enables Lunar Spacecraft,

- Journal of Mechanical Design, 139, 2017. <https://doi.org/10.1115/1.4037304>.
- [14] Plocher, J.; Panesar, A.: Review on design and structural optimisation in additive manufacturing: Towards next-generation lightweight structures, *Materials and Design*, 183, 2019. <https://doi.org/10.1016/j.matdes.2019.108164>.
- [15] Wang, Y.; Sigmund, O.: Topology optimization of multi-material active structures to reduce energy consumption and carbon footprint, *Structural and Multidisciplinary Optimization*, 67, 2024. <https://doi.org/10.1007/s00158-023-03698-3>.
- [16] Duysinx, P.; Bendsøe, M. P.: Topology optimization of continuum structures with local stress constraints, *International Journal for Numerical Methods in Engineering*, 43, 1998, 1453–1478. [https://doi.org/10.1002/\(SICI\)1097-0207\(19981230\)43:8<1453::AID-NME480>3.0.CO;2-2](https://doi.org/10.1002/(SICI)1097-0207(19981230)43:8<1453::AID-NME480>3.0.CO;2-2).
- [17] Le, C.; Norato, J.; Bruns, T.; Ha, C.; Tortorelli, D.: Stress-based topology optimization for continua, *Structural and Multidisciplinary Optimization*, 41(4), 2010, 605–620. <https://doi.org/10.1007/s00158-009-0440-y>.
- [18] Xia, L.; Zhang, L.; Xia, Q.; Shi, T.: Stress-based topology optimization using bi-directional evolutionary structural optimization method, *Computer Methods in Applied Mechanics and Engineering*, 333, 2018, 356–370. <https://doi.org/10.1016/j.cma.2018.01.035>.
- [19] Conlan-Smith, C.; James, K. A.: A stress-based topology optimization method for heterogeneous structures, *Structural and Multidisciplinary Optimization*, 60, 2019, 167–183. <https://doi.org/10.1007/s00158-019-02207-9>.
- [20] Holmberg E.; Torstenfelt B.; Klarbring A.: Stress-constrained topology optimization, *Structural and Multidisciplinary Optimization*, 48(1), 2013, 33–47. <https://doi.org/10.1007/s00158-012-0880-7>.
- [21] Guo, X.; Zhang, W. S.; Wang, M. Y.; Wei, P.: Stress-related topology optimization via level set approach, *Computer Methods in Applied Mechanics and Engineering*, 200(47–48), 2011, 3439–3452. <https://doi.org/10.1016/j.cma.2011.08.016>.
- [22] Zhang, W.; Li, D.; Zhou, J.; Du, Z.; Li, B.; Guo, X.: A Moving Morphable Void (MMV)-based explicit approach for topology optimization considering stress constraints, *Computer Methods in Applied Mechanics and Engineering*, 334, 2018, 381–413. <https://doi.org/10.1016/j.cma.2018.01.050>.
- [23] Deng, H.; Cheng, L.; C. To, A.: Distortion energy-based topology optimization design of hyperelastic materials, *Structural and Multidisciplinary Optimization*, 59(6), 2019, 1895–1913. <https://doi.org/10.1007/s00158-018-2161-6>.
- [24] Xu, S.; Liu, J.; Zou, B.; Li, Q.; Ma, Y.: Stress constrained multi-material topology optimization with the ordered SIMP method, *Computer Methods in Applied Mechanics and Engineering*, 373, 2021, 113453. <https://doi.org/10.1016/j.cma.2020.113453>.
- [25] Han, Z.; Wei, K.; Gu, Z.; Ma, X.; Yang, X.: Stress-constrained multi-material topology optimization via an improved alternating active-phase algorithm, *Engineering Optimization*, 54(2), 2022, 305–328. <https://doi.org/10.1080/0305215X.2020.1867119>.
- [26] Cheng, L.; Bai, J.; To, A. C.: Functionally graded lattice structure topology optimization for the design of additive manufactured components with stress constraints, *Computer Methods in Applied Mechanics and Engineering*, 344, 2019, 334–359. <https://doi.org/10.1016/j.cma.2018.10.010>.
- [27] Yu, H.; Huang, J.; Zou, B.; Shao, W.; Liu, J.: Stress-constrained shell-lattice infill structural optimisation for additive manufacturing, *Virtual and Physical Prototyping*, 15(1), 2020, 35–48. <https://doi.org/10.1080/17452759.2019.1647488>.
- [28] Thillaithevan, D.; Bruce, P.; Santer, M.: Stress-constrained optimization using graded lattice microstructures, *Structural and Multidisciplinary Optimization*, 63(2), 2021, 721–740. <https://doi.org/10.1007/s00158-020-02723-z>.
- [29] Wu, J.; Aage, N.; Westermann, R.; Sigmund, O.: Infill Optimization for Additive Manufacturing-Approaching Bone-Like Porous Structures, *IEEE Transactions on Visualization and Computer Graphics*, 24(2), 2018, 1127–1140. <https://doi.org/10.1109/TVCG.2017.2655523>.

- [30] Liu, X.; Shapiro, V.: Random heterogeneous materials via texture synthesis, *Computational Materials Science*, 99, 2015, 177–189. <https://doi.org/10.1016/j.commatsci.2014.12.017>
- [31] Wei, L.-Y.; Lefebvre, S.; Kwatra, V.; Turk, G.: State of the Art in Example-based Texture Synthesis, The Eurographics Association, 2009. <http://dx.doi.org/10.2312/egst.20091063>.
- [32] Huiskes R.; Ruimerman R.; van Lenthe, G. H.; Janssen J.D.: Effects of mechanical forces on maintenance and adaptation of form in trabecular bone, *Nature*. 405(6787), 2000, 704–706. <https://doi.org/10.1038/35015116>.
- [33] Coelho, P. G.; Fernandes, P. R.; Rodrigues, H. C.; Cardoso, J. B.; Guedes, J. M.: Numerical modeling of bone tissue adaptation—A hierarchical approach for bone apparent density and trabecular structure, *Journal of Biomechanics*, 42(7), 2009, 830–837. <https://doi.org/10.1016/j.jbiomech.2009.01.020>.
- [34] Wang, X.; Xu, S.; Zhou, S.; Xu, W.; Leary, M.; Choong, P.; Qian, M.; Brandt, M.; Xie, Y. M.: Topological design and additive manufacturing of porous metals for bone scaffolds and orthopaedic implants: A review, *Biomaterials*, 83, 2016, 127–141. <https://doi.org/10.1016/j.biomaterials.2016.01.012>.
- [35] Schury, F.; Stingl, M.; Wein, F.: Efficient Two-Scale Optimization of Manufacturable Graded Structures, *SIAM Journal on Scientific Computing*, 34(6), 2012, B711–B733. <https://doi.org/10.1137/110850335>.
- [36] Groen, J. P.; Sigmund, O.: Homogenization-based topology optimization for high-resolution manufacturable microstructures, *International Journal for Numerical Methods in Engineering*, 113(8), 2018, 1148–1163. <https://doi.org/10.1002/nme.5575>.
- [37] Wu J.; Wang W.; Gao X.: Design and Optimization of Conforming Lattice Structures, *IEEE Transactions on Visualization and Computer Graphics*, vol. 27, no. 1, pp. 43-56, 2021. <https://doi.org/10.1109/TVCG.2019.2938946>.
- [38] Frillici F.S.; Rotini F.: Prosthesis Socket Design through Shape Optimization, *Computer-Aided Design and Applications*, 10(5), 2013, 863-876. <https://doi.org/10.3722/cadaps.2013.863-876>.
- [39] Daynes, S.; Feih, S.; Lu, W. F.; Wei, J.: Design concepts for generating optimised lattice structures aligned with strain trajectories, *Computer Methods in Applied Mechanics and Engineering*, 354, 2019, 689–705. <https://doi.org/10.1016/j.cma.2019.05.053>.
- [40] Daynes, S.; Feih, S.: Bio-inspired lattice structure optimisation with strain trajectory aligned trusses, *Materials and Design*, 213, 2022. <https://doi.org/10.1016/j.matdes.2021.110320>.
- [41] Zuo, W.; Saitou, K.: Multi-material topology optimization using ordered SIMP interpolation, *Structural and Multidisciplinary Optimization*, 55(2), 2017, 477–491. <https://doi.org/10.1007/s00158-016-1513-3>.